H1prelim-08-173 Submitted to

34th International Conference on High Energy Physics, ICHEP2008, 30th July - 5th August, Philadelphia

Abstract: **834**

Parallel Session **QCD/Lattice**

Electronic Access:https://www-h1.desy.de/publications/H1preliminary.short_list.html

Measurement of $F_2^{c\bar{c}}$ and $F_2^{b\bar{b}}$ using the H1 Vertex Detector at HERA

H1 Collaboration

Abstract

The inclusive charm and beauty cross sections are measured in e^-p and e^+p collisions at HERA II in the kinematic region of photon virtuality $5 \leq Q^2 \leq 650\ \mathrm{GeV}^2$ and Bjorken scaling variable $0.0002 \leq x \leq 0.032$. The data were collected with the H1 detector in 2006 and 2007 corresponding to an integrated luminosity of 189 pb^{-1}. The charm and beauty fractions are determined using a neural network which includes inputs, as measured by the H1 vertex detector, of the impact parameter of tracks to the primary vertex and the position of the secondary vertex. The measurements are compared with previous data, NLO and NNLO QCD predictions.

1 Introduction

In this paper measurements of the charm (c) and beauty (b) contributions to the inclusive proton structure function F_2 are made in Deep Inelastic Scattering (DIS) at HERA, using information from the H1 vertex detector, for values of the negative square of the four momentum of the exchanged boson $5 \leq Q^2 \leq 650\ \mathrm{GeV}^2$, and of Bjorken x, $0.0002 \leq x \leq 0.032$. The analysis extends to lower Q^2 than has been previously measured by H1 using this technique [1, 2]. The analysis is based on a sample of neutral current scattering data, taken in the years 2006-2007, with an integrated luminosity of $189\ \mathrm{pb}^{-1}$ with $53\ \mathrm{pb}^{-1}$ in e^-p mode and $135\ \mathrm{pb}^{-1}$ in e^+p mode. The ep centre of mass energy is $\sqrt{s} = 319\ \mathrm{GeV}$, with a proton beam energy of $920\ \mathrm{GeV}$. Many details of the analysis are similar to that used by H1 in measurements of HERA I data [1, 2].

Events containing heavy quarks are distinguished from those containing only light quarks using a neural network (NN), which has input variables which are reconstructed from the H1 vertex detector. The most important of these inputs are the transverse displacement of tracks from the primary vertex and the reconstructed position of a secondary vertex in the transverse plane. This method has better descrimination between c and b compared to previous methods [1, 2], which used only the transverse displacement of tracks from the primary vertex. The measurement is made differentially by dividing the data into discrete y–Q^2 intervals. The charm structure function $F_2^{c\bar{c}}$ and the beauty structure function $F_2^{b\bar{b}}$ are obtained from the measured c and b cross sections after small corrections for the longitudinal structure functions $F_L^{c\bar{c}}$ and $F_L^{b\bar{b}}$.

2 Monte Carlo Simulation

Monte Carlo simulations are used to correct for the effects of the finite detector resolution, acceptance and efficiency. The Monte Carlo program RAPGAP [3] is used to generate DIS events for the processes $ep \to eb\bar{b}X$, $ep \to ec\bar{c}X$ and $ep \to eqX$ where q is a light quark of flavour u, d or s. RAPGAP combines $\mathcal{O}(\alpha_s)$ matrix elements with higher order QCD effects modelled by the emission of parton showers. The heavy flavour event samples are generated according to the massive photon gluon fusion (PGF) matrix element with the mass of the c and b quarks set to $m_c = 1.5\ \mathrm{GeV}$ and $m_b = 4.75\ \mathrm{GeV}$, respectively. The DIS cross section is calculated using the leading order (LO) 3-flavour parton distribution functions (PDFs) from [4].

The partonic system for the generated events is fragmented according to the LUND string model implemented within the PYTHIA program [6]. The c and b quarks are hadronised according to the Bowler fragmentation function [5]. The HERACLES program [7] calculates single photon radiative emissions off the lepton line, virtual and electroweak corrections.

The samples of events generated for the uds, c, and b processes are passed through a detailed simulation of the detector response based on the GEANT3 program [8], and through the same reconstruction software as is used for the data.

3 H1 Detector

Only a short description of the H1 detector is given here; a full description may be found in [9]. A right handed coordinate system is employed at H1 that has its z-axis pointing in the proton beam, or forward, direction and x (y) pointing in the horizontal (vertical) direction.

Charged particles are measured in the central tracking detector (CTD). This device consists of two cylindrical drift chambers interspersed with z-chambers to improve the z-coordinate reconstruction and multi–wire proportional chambers mainly used for triggering. The CTD is situated in a uniform $1.15\,\mathrm{T}$ magnetic field, enabling momentum measurement of charged particles over the polar angular range[1] $20^\circ < \theta < 160^\circ$.

The CTD tracks are linked to hits in the vertex detector (central silicon tracker CST) [10] to provide precise spatial track reconstruction. The CST consists of two layers of double-sided silicon strip detectors surrounding the beam pipe, covering an angular range of $30^\circ < \theta < 150^\circ$ for tracks passing through both layers. The information on the z-coordinate of the CST tracks is not used in the analysis presented in this paper. For CTD tracks with CST hits in both layers the transverse distance of closest approach (DCA) to the nominal vertex in x–y can be measured with a resolution of $33\ \mu\mathrm{m} \oplus 90\ \mu\mathrm{m}/p_T[\mathrm{GeV}]$, where the first term represents the intrinsic resolution (including alignment uncertainty) and the second term is the contribution from multiple scattering in the beam pipe and the CST; p_T is the transverse momentum of the track.

The track detectors are surrounded in the forward and central directions ($4^\circ < \theta < 155^\circ$) by a fine grained liquid argon calorimeter (LAr) and in the backward region ($153^\circ < \theta < 178^\circ$) by a lead–scintillating fibre calorimeter (SPACAL) [11] with electromagnetic and hadronic sections. These calorimeters provide energy and angular reconstruction for final state particles from the hadronic system and are also used in this analysis to measure and identify the scattered electron.

Electromagnetic calorimeters situated downstream in the electron beam direction allow detection of photons and electrons scattered at very low Q^2. The luminosity is measured from the rate of photons produced in the Bethe-Heitler process $ep \to ep\gamma$.

4 Experimental Method

4.1 Event Selection

The events are selected by requiring a compact electromagnetic cluster in either the LAr or SPACAL calorimeters, which is taken as the scattered electron. The z-position of the interaction vertex, reconstructed by one or more charged tracks in the tracking detectors, must be within ± 20 cm of the centre of the detector to match the acceptance of the CST. Photoproduction events are suppressed by requiring $\sum_i (E_i - p_{z,i}) > 35$ GeV. Here, E_i and $p_{z,i}$ denote the energy and longitudinal momentum components of a particle and the sum is over all final state particles including the scattered electron and the hadronic final state (HFS). The HFS particles

[1] The angular coverage of each detector component is given for the interaction vertex in its nominal position.

are reconstructed using a combination of tracks and calorimeter deposits in an energy flow algorithm that avoids double counting. The event kinematics, Q^2 and the inelasticity variable y, are reconstructed with the '$e\Sigma$' method [12], which uses the scattered electron and the HFS. The Bjorken scaling variable x is obtained from $x = Q^2/sy$. In order to have good acceptance in the SPACAL and to ensure that the HFS has a significant transverse momentum, events are selected in the range $4.5 < Q^2 < 1585\ \mathrm{GeV}^2$. The analysis is restricted to $0.07 < y < 0.625$ to ensure that the direction of the quark which is struck by the photon is mostly in the CST angular range and to reduce photoproduction background.

The position of the beam interaction region, calculated at regular time intervals using information from tracks with CST hits, is used as the position of the primary event vertex in r–ϕ.

4.2 Track Selection

The impact parameter of a track, which is the transverse distance of closest approach (DCA) of the track to the primary vertex point, is only determined for those tracks which are measured in the CTD and have at least two CST hits linked (referred to as CST tracks). CST tracks are required to have a transverse momentum > 0.3 GeV.

The impact parameter (δ) of a track with respect to the primary vertex is signed according to the azimuthal angle of the struck quark ϕ_{quark}. The quantity ϕ_{quark} is reconstructed as the azimuthal angle of the highest p_T jet in the event or, if there is no jet reconstructed in the event, as $180^\circ - \phi_{\mathrm{elec}}$, where ϕ_{elec} is the azimuthal angle of the electron in degrees. Jets are are reconstructed using the invariant k_T algorithm [13] in the laboratory frame using all reconstructed HFS particles and are required to have $p_T > 1.5$ GeV, in the angular range $15^\circ < \theta < 155^\circ$. Approximately 95% (99%) of c (b) events have ϕ_{quark} reconstructed from a jet, as determined from the Monte Carlo simulation.

If the angle between the quark axis and the line joining the primary vertex to the point of DCA is less than 90°, δ is defined as positive, and is defined as negative otherwise. Tracks with azimuthal angle outside $\pm 90^\circ$ of ϕ_{quark} are assumed not to be associated to the quark axis and rejected. The δ distribution, shown in figure 1, is seen to be asymmetric with positive values in excess of negative values indicating the presence of long lived particles. It is found to be well described by the Monte Carlo simulation. For the track significance distributions and the NN inputs we reject tracks with $|\delta| > 0.1$ cm to suppress light quark events containing long lived strange particles.

4.3 Secondary Vertex Reconstruction

The tracks in the event are used to simultaneously reconstruct a secondary and primary vertex in the transverse plane. Each track is assigned a weight for each vertex, which is a measure of the probability that the track originated at that vertex [14]. In this approach tracks are not assigned unambiguously to one vertex or the other. A simultaneous fit to the primary and secondary vertex is made, with the weights of all tracks of the event considered for the primary vertex, but only the weights of those tracks associated to the quark axis considered for the secondary vertex. The vertex configuration that minimises the global χ^2 is found iteratively using deterministic annealing [15].

The transverse distance between the secondary and primary vertex is defined as L_{xy}. The secondary vertex significance S_L is $L_{xy}/\sigma(L_{xy})$, where $\sigma(L_{xy})$ is the error on L_{xy}. If the absolute difference between the azimuthal angle of the secondary vertex (taking the primary vertex as the origin) and the quark axis is less than $90°$, S_L is signed positive and negative otherwise. A measure of the decay multiplicity N_{sec} is made by counting the number of tracks with weight > 0.8 to the seondary vertex.

4.4 Quark Flavour Separation

In [1] and [2] track significances ($\delta/\sigma(\delta)$, where $\sigma(\delta)$ is the error on δ) were used to distinguish between the c, b and light quark flavours. The significances S_1, S_2 and S_3, are defined as the significance of the track with the highest, second highest and third highest absolute significance, respectively. In [1] it was also shown that consistent results were obtained using a reconstructed secondary vertex in the transverse plane. In the present analysis we use S_1 for events with only 1 reconstructed CST track and S_2 for events with 2 CST tracks; for events with ≥ 3 CST tracks we combine information from the significance distributions and the reconstructed secondary vertex using a NN that combines the information in an optimal way, taking into account correlations of the input variables [16]. Events in which S_1 and S_2 have opposite signs are excluded from the S_2 distribution. Events in which S_1 and S_2 or S_3 do not all have the same sign are excluded from the NN distribution. The S_1 and S_2 distributions for 1 and 2 CST track events, respectively, are shown in figure 2.

The NN has inputs of S_1, S_2, S_3, S_L, the transverse momentum of the CST track with the highest and second highest transverse momentum, the number of CST tracks, and the number of CST tracks associated to the secondary vertex. The NN has one hidden layer with 5 nodes. It was trained using a sample of around 2000 Monte Carlo b events as 'signal' and a similar number of Monte Carlo c events as 'background'. The distributions of the NN inputs are shown in figures 3 and 4. These distributions are dominated by light quark events. It can be seen that the Monte Carlo gives a good description of these distributions. It is also apparent that these distributions have good separation power between light, c and b events. The decrease in events around zero for the S_1 and S_2 distributions is due to the requirement that $S_1 > S_2 > S_3$. In order to check the heavy flavour contribution we take the distributions of those events with $S_2 > 2$ and subtract off the corresponding distributions for those events with $S_2 < -2$. These subtracted distributions are shown in figure 5. The Monte Carlo also gives a good description of these distributions.

The output of the NN is shown in figure 6. The NN output is signed according to the sign of the most significant track. It can be seen that the light quark distribution is approximately symmetric and peaks towards low values; c and b are asymmetric with more positive than negative entries; the b events are peaked towards 1, whereas the c events are peaked towards 0. The Monte Carlo gives a good description of the distribution.

In order to reduce the uncertainty due to the resolution of δ and the light quark normalisation, the contents of the negative bins in the S_1, S_2 and NN distributions are subtracted from the contents of the corresponding positive bins. The subtracted distributions are shown in figure 7. It can be seen that the resulting distributions are dominated by c quark events, with a b quark fraction increasing towards the upper end of the distributions. The light quarks contribute a small fraction.

The fractions of c, b and light quarks of the data are extracted in each y–Q^2 interval using a least squares simultaneous fit to the subtracted S_1, S_2 and NN distributions (as in figure 7) and the total number of inclusive events before any CST track selection. The c, b and uds Monte Carlo simulation samples are used as templates. The Monte Carlo c, b and uds contributions in each y–Q^2 interval are scaled by factors ρ_c, ρ_b and ρ_l, respectively, to give the best fit to the observed subtracted S_1, S_2 and NN distributions and the total number of inclusive events. Only the statistical errors of the data and Monte Carlo simulation are considered in the fit. The fit to the subtracted significance and NN distributions mainly constrains ρ_c and ρ_b, whereas the overall normalisation constrains ρ_l.

The results of the fit to the complete data sample are shown in figure 7. The fit gives a reasonable description of all the significance distributions, with a $\chi^2/n.d.f$ of $98/48$, with only statistical errors taken into account. The c and b scale factors are found to be anti-correlated with an overall correlation coefficient of -0.61. Acceptable χ^2 values are also found for the fits to the samples in the separate y–Q^2 intervals.

The results of the fit in each y–Q^2 interval are converted to a measurement of the 'reduced c cross section' defined from the differential cross section as

$$\tilde{\sigma}^{c\bar{c}}(x, Q^2) = \frac{\mathrm{d}^2\sigma^{c\bar{c}}}{\mathrm{d}x\,\mathrm{d}Q^2} \frac{xQ^4}{2\pi\alpha^2(1 + (1-y)^2)}, \tag{1}$$

using:

$$\tilde{\sigma}^{c\bar{c}}(x, Q^2) = \tilde{\sigma}(x, Q^2) \frac{\rho_c N_c^{\mathrm{MCgen}}}{\rho_c N_c^{\mathrm{MCgen}} + \rho_b N_b^{\mathrm{MCgen}} + \rho_l N_l^{\mathrm{MCgen}}} \delta_{\mathrm{BCC}}, \tag{2}$$

where $\tilde{\sigma}(x, Q^2)$ is the measured inclusive reduced cross section from H1([17] for $Q^2 \leq 60\,\mathrm{GeV}^2$, otherwise [18]) and N_c^{MCgen}, N_b^{MCgen} and N_l^{MCgen} are the number of c, b and light quark events generated from the Monte Carlo in each bin. A bin centre correction δ_{BCC} is applied using a NLO QCD expectation for $\tilde{\sigma}^{c\bar{c}}$ to convert the bin averaged measurement into a measurement at a given x–Q^2 point. The NLO QCD expectation is calculated from the results of a fit similar to that performed in [19] but using the FFNS scheme to generate heavy flavours. A small correction ($\leq 2.6\%$) for the beam energy difference is applied, using the NLO QCD expectation, to the measurement of $\tilde{\sigma}(x, Q^2)$ with $Q^2 \leq 60$ GeV^2 which was performed at a lower centre of mass energy of 301 GeV than the data presented here. The cross section is defined so as to include a correction for pure QED radiative effects. Events that contain c hadrons via the decay of b hadrons are not included in the definition of the c cross section. The differential b cross section is evaluated in the same manner.

Since the error on ρ_c is much smaller than that of ρ_b we are able to measure the c cross section in more y–Q^2 intervals than the b cross section. We therefore perform two sets of fits (as described above): one with a finer binning from which we extract $\tilde{\sigma}^{c\bar{c}}$; and the other with a coarser binning from which we extract $\tilde{\sigma}^{b\bar{b}}$. The two sets of fits are performed in an identical manner.

5 Results

The measurements of $\tilde{\sigma}^{c\bar{c}}$ are shown as a function of x for fixed values of Q^2 in figure 8 and of $\tilde{\sigma}^{b\bar{b}}$ in figure 9. Also shown in these figures are the HERA I data extracted using measurements based on the displacement of tracks. The $\tilde{\sigma}^{c\bar{c}}$ and $\tilde{\sigma}^{b\bar{b}}$ data from HERA I and HERA II show good agreement for all measured x and Q^2 values. The $\tilde{\sigma}^{b\bar{b}}$ results are averaged using the method of [20]. In this method the correlation between the systematic errors of the data points are taken into account. The averaged measurements are also shown in figure 9. The $\tilde{\sigma}^{c\bar{c}}$ are compared with those extracted from D^* meson measurements by H1 [21], obtained using a NLO program [22] based on DGLAP evolution to extrapolate the measurements outside the visible D^* range. The D^* data agree well with the measurements from the present analysis.

The $\tilde{\sigma}^{c\bar{c}}$ data are compared in figure 10 with two recent predictions from NLO QCD based on the variable flavour number scheme (VFNS) from MSTW [23] and CTEQ [24], and with predictions based on CCFM [25] parton evolution. The predictions provide a reasonable description of the present data.

The $\tilde{\sigma}^{b\bar{b}}$ data are compared in figure 11 with the two VFNS NLO QCD predictions and the CCFM prediction. The data are well described by the predictions including the point in the extended data region at $Q^2 = 5\ \mathrm{GeV}^2$.

The structure function $F_2^{c\bar{c}}$ is evaluated from the reduced cross section

$$\tilde{\sigma}^{c\bar{c}} = F_2^{c\bar{c}} - \frac{y^2}{1+(1-y)^2} F_L^{c\bar{c}}, \tag{3}$$

where the longitudinal structure function $F_L^{c\bar{c}}$ is estimated from the same NLO QCD expectation as used for the bin centre correction. The structure function $F_2^{b\bar{b}}$ is evaluated in the same manner.

The measurements of $F_2^{b\bar{b}}$ are shown as a function of Q^2 in figure 13. The data are compared with the VFNS QCD predictions from MSTW at NLO and a calculation at NNLO [23, 26].

6 Conclusion

The differential charm and beauty cross sections in Deep Inelastic Scattering are measured for a wide range of Q^2 and Bjorken x using the impact parameters and the position of the secondary vertex as reconstructed from the vertex detector using the HERA II data. The cross sections and derived structure functions $F_2^{c\bar{c}}$ and $F_2^{b\bar{b}}$ have reduced errors and agree with previous measurements. The measurements are described by predictions using perturbative QCD.

References

[1] A. Aktas *et al.* [H1 Collaboration], Eur. Phys. J. C **40** (2005) 349 [hep-ex/0411046].

[2] A. Aktas *et al.* [H1 Collaboration], Eur. Phys. J. C **45** (2006) 23 [hep-ex/0507081].

[3] H. Jung, Comput. Phys. Commun. **86** (1995) 147;
(see also http://www.desy.de/∼jung/rapgap/).

[4] A. D. Martin, W. J. Stirling and R. S. Thorne, Phys. Lett. B **636** (2006) 259 [hep-ph/0603143].

[5] M. G. Bowler, Z. Phys.C **11** (1981) 169.

[6] T. Sjöstrand, L. Lönnblad and S. Mrenna, hep-ph/0108264.

[7] A. Kwiatkowski, H. Spiesberger and H. J. Möhring, Comput. Phys. Commun. **69** (1992) 155.

[8] R. Brun, R. Hagelberg, M. Hansroul and J. C. Lassalle, CERN-DD-78-2-REV.

[9] I. Abt *et al.* [H1 Collaboration], Nucl. Instrum. Meth. A **386** (1997) 310 and 348.

[10] D. Pitzl *et al.*, Nucl. Instrum. Meth. A **454** (2000) 334 [hep-ex/0002044].

[11] T. Nicholls *et al.* [H1 SPACAL Group], Nucl. Instrum. Meth. A **374** (1996) 149.

[12] U. Bassler and G. Bernardi, Nucl. Instrum. Meth. A **361** (1995) 197 [hep-ex/9412004].

[13] S. D. Ellis and D. E. Soper, Phys. Rev. D **48** (1993) 3160 [hep-ph/9305266];

S. Catani, Y. L. Dokshitzer, M. H. Seymour and B. R. Webber, Nucl. Phys. B **406** (1993) 187.

[14] R. Frühwirth *et al.*, Nucl. Instrum. Meth. A **502** (2003) 699.

[15] R. Frühwirth and A. Strandlie, Comput. Phys. Commun. **120** (1999) 197.

[16] C. Peterson, T. Rognvaldsson and L. Lönnblad, Comput. Phys. Commun. **81** (1994) 185.

[17] C. Adloff *et al.* [H1 Collaboration], Eur. Phys. J. C **21** (2001) 33 [hep-ex/0012053].

[18] C. Adloff *et al.* [H1 Collaboration], Eur. Phys. J **C 30** (2003) 1 [hep-ex/0304003].

[19] C. Adloff *et al.* [H1 Collaboration], Eur. Phys. J. C **13** (2000) 609 [hep-ex/9908059].

[20] A. Glazov, "Averaging of DIS cross section data", AIP Conf. Proc. **792** (2005) 237.

[21] H1 Collaboration, "Dstar production at low Q2 with the H1 detector", contribution to the 16^{th} International Conference on Deep-inelastic Scattering (DIS08), London UK, April 2008;

H1 Collaboration, "Dstar production at high Q2 with the H1 detector", contribution to the 34^{th} International Conference on High Energy Physics, Philadelphia USA, July 2007.

[22] B. W. Harris and J. Smith, Phys. Rev. D **57** (1998) 2806 [hep-ph/9706334].

[23] G. Watt, A. D. Martin, W. J. Stirling and R. S. Thorne, arXiv:0806.4890 [hep-ph].

[24] P. M. Nadolsky *et al.*, arXiv:0802.0007 [hep-ph].

[25] H. Jung, "Unintegrated PDFs in CCFM", proceedings of 12$^{\text{th}}$ International Workshop on Deep Inelastic Scattering (DIS 2004), Strbske Pleso, Slovakia, 2004 [hep-ph/0411287];

M. Ciafaloni, Nucl. Phys. B **296** (1988) 49;

S. Catani, F. Fiorani and G. Marchesini, Phys. Lett. B **234** (1990) 339;

S. Catani, F. Fiorani and G. Marchesini, Nucl. Phys. B **336** (1990) 18;

G. Marchesini, Nucl. Phys. B **445** (1995) 49 [hep-ph/9412327].

[26] R. S. Thorne, Phys. Rev. D **73** (2006) 054019 [hep-ph/0601245].

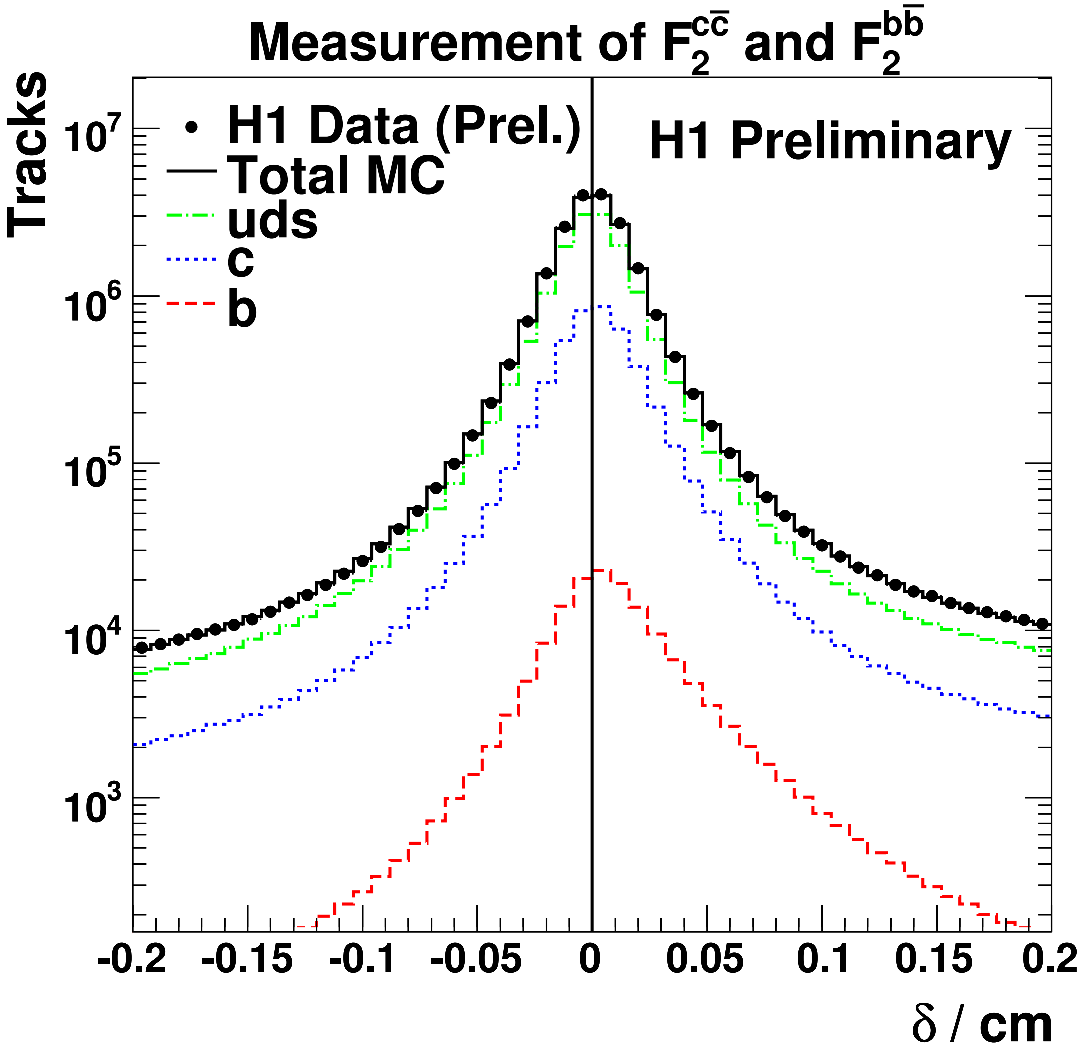

Figure 1: The distribution of the signed impact parameter δ of a track to the primary vertex in the x–y plane. Included in the figure is the expectation from the Monte Carlo simulation for light, c and b quarks. The contributions from the various quark flavours are shown after applying the scale factors obtained from the fit to the subtracted significance distributions of the data (see section 4.4).

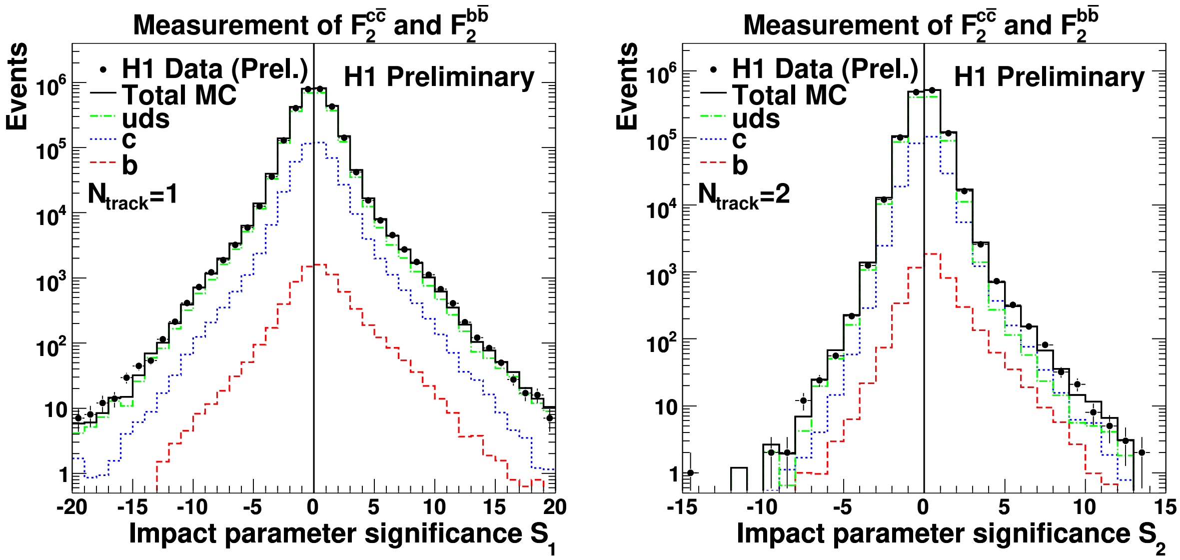

Figure 2: The significance $\delta/\sigma(\delta)$ distribution (a) of the highest absolute significance track (S_1) for 1 track events and (b) of the track with the second highest absolute significance (S_2). Included in the figure is the expectation from the Monte Carlo simulation for light, c and b quarks. The contributions from the various quark flavours are shown after applying the scale factors obtained from the fit to the data.

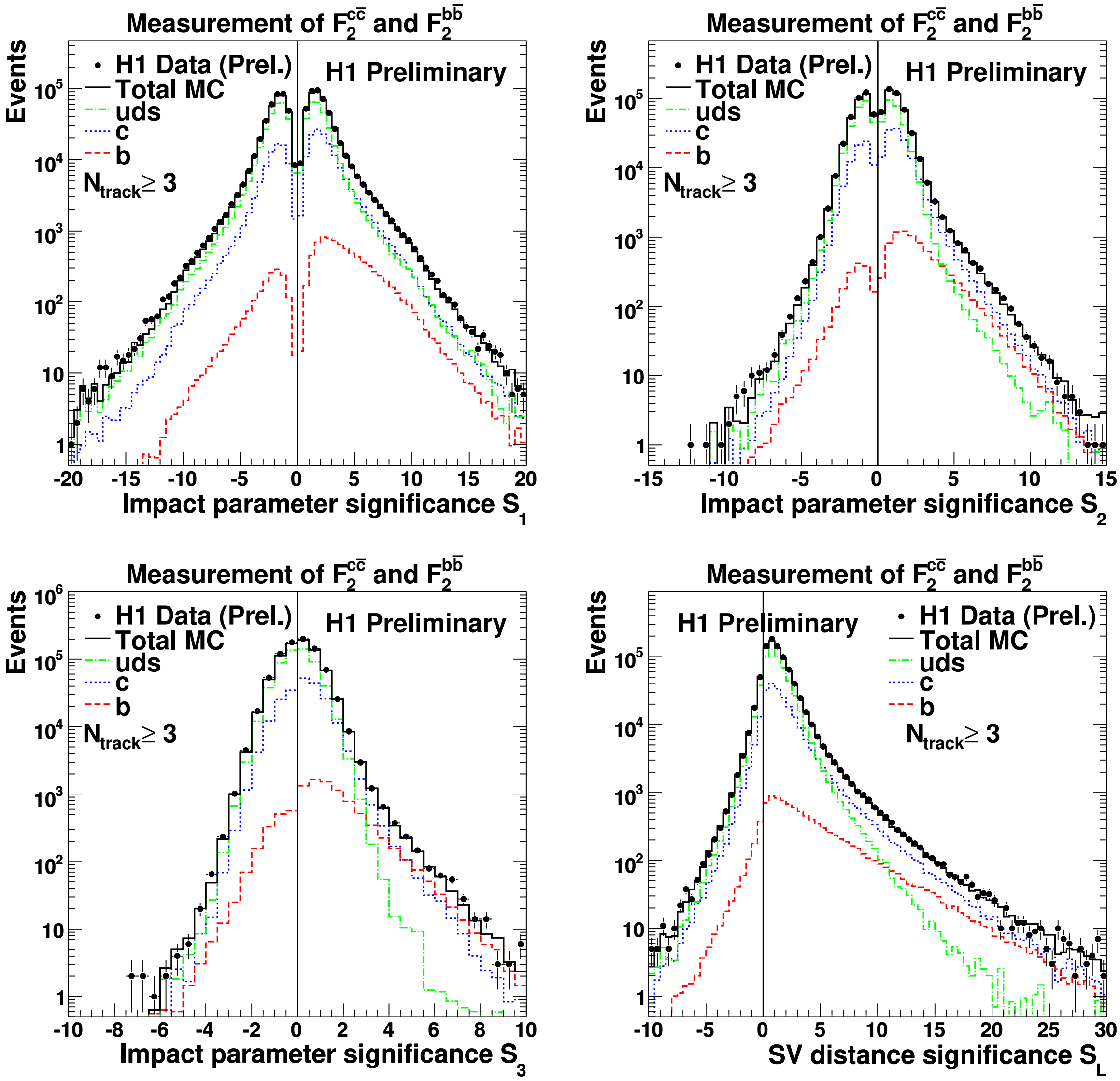

Figure 3: The first four inputs to the NN. Included in the figure is the expectation from the Monte Carlo simulation for light, c and b quarks. The contributions from the various quark flavours are shown after applying the scale factors obtained from the fit the data.

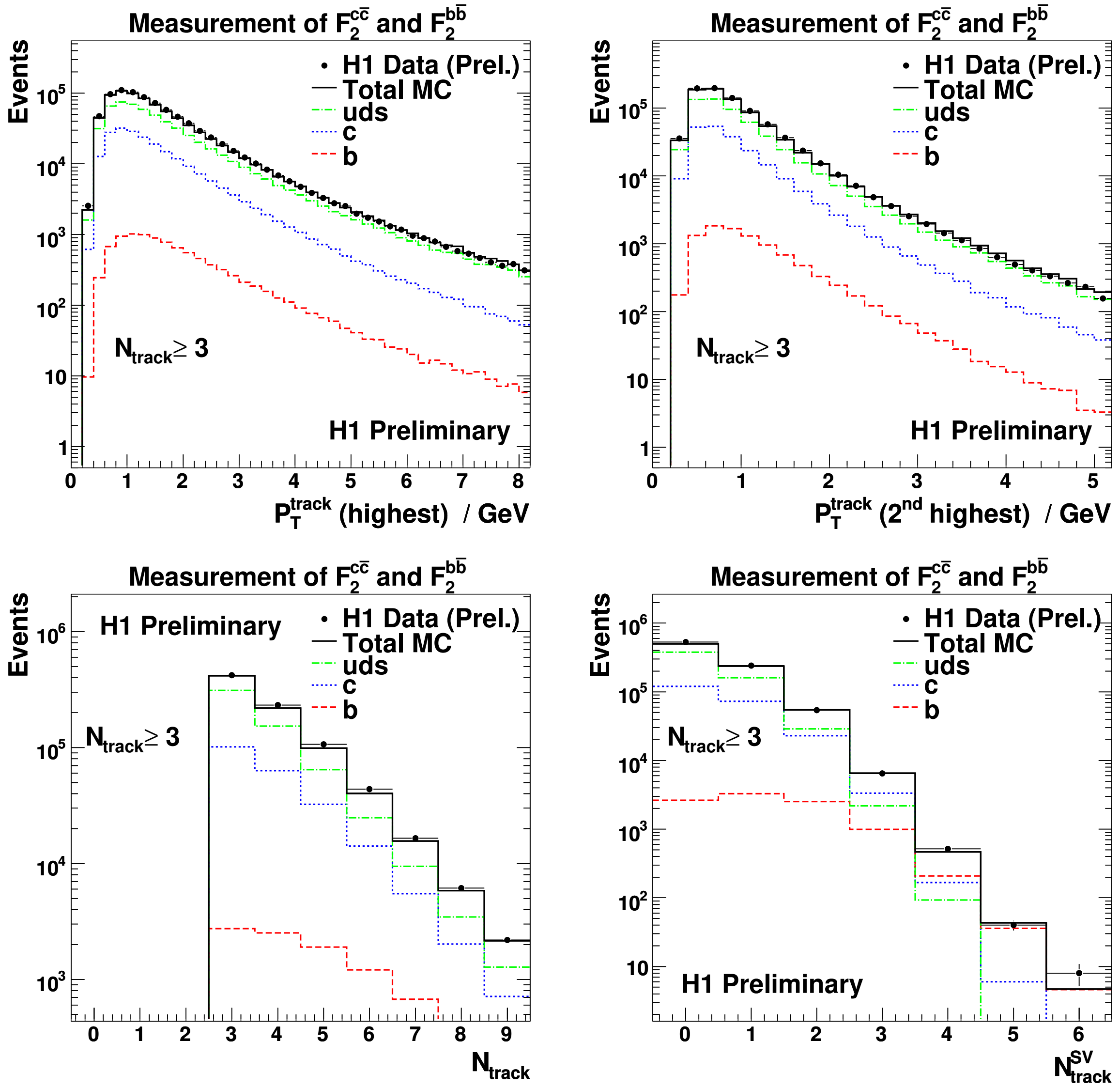

Figure 4: The second four inputs to the NN. Included in the figure is the expectation from the Monte Carlo simulation for light, c and b quarks. The contributions from the various quark flavours are shown after applying the scale factors obtained from the fit to the data.

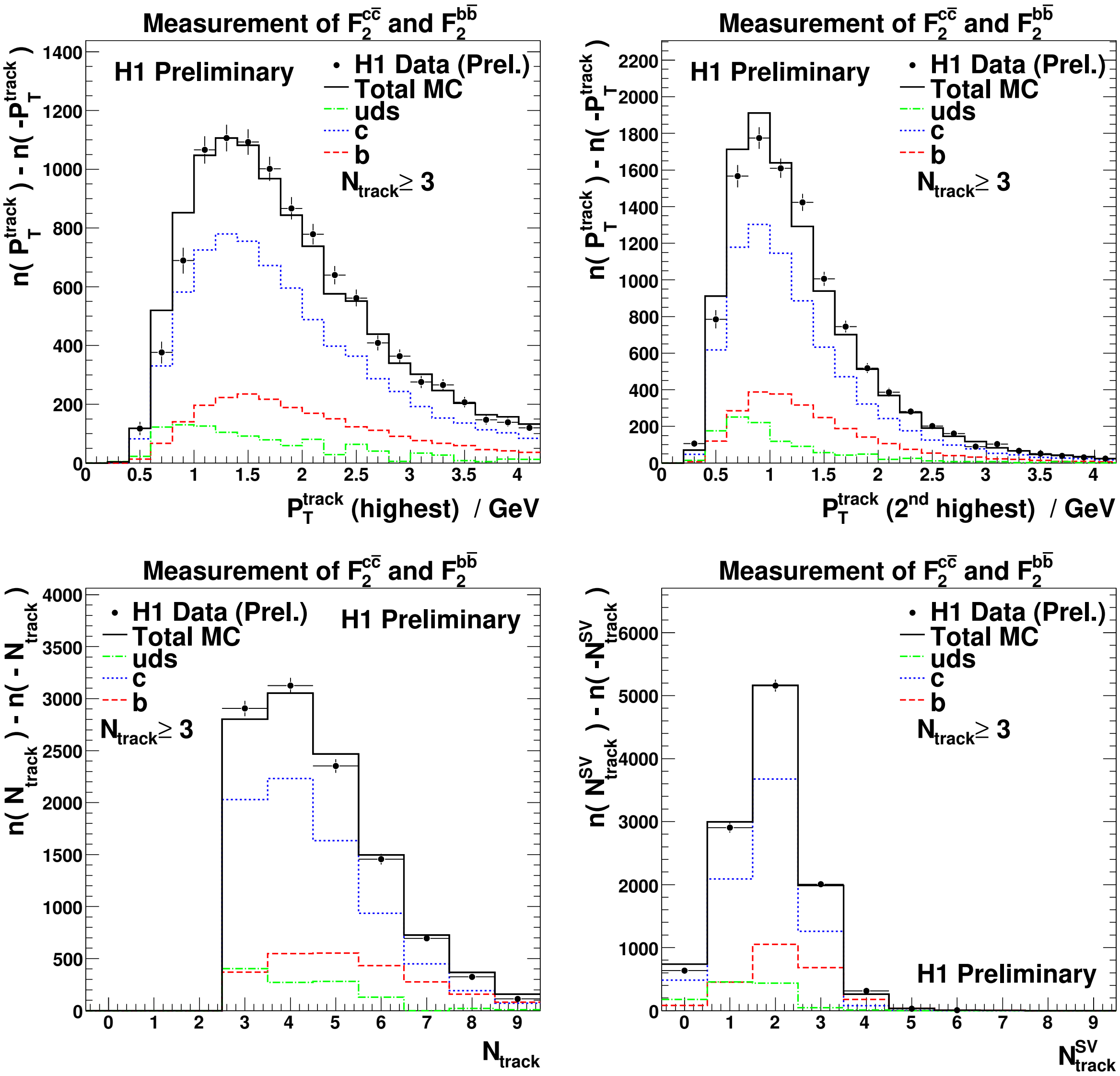

Figure 5: The subtracted distributions for the transverse momentum of the highest and second highest transverse momentum track, the number of tracks and the number of tracks assigned to the secondary vertex. Included in the figure is the expectation from the Monte Carlo simulation for light, c and b quarks. The contributions from the various quark flavours are shown after applying the scale factors obtained from the fit to the data.

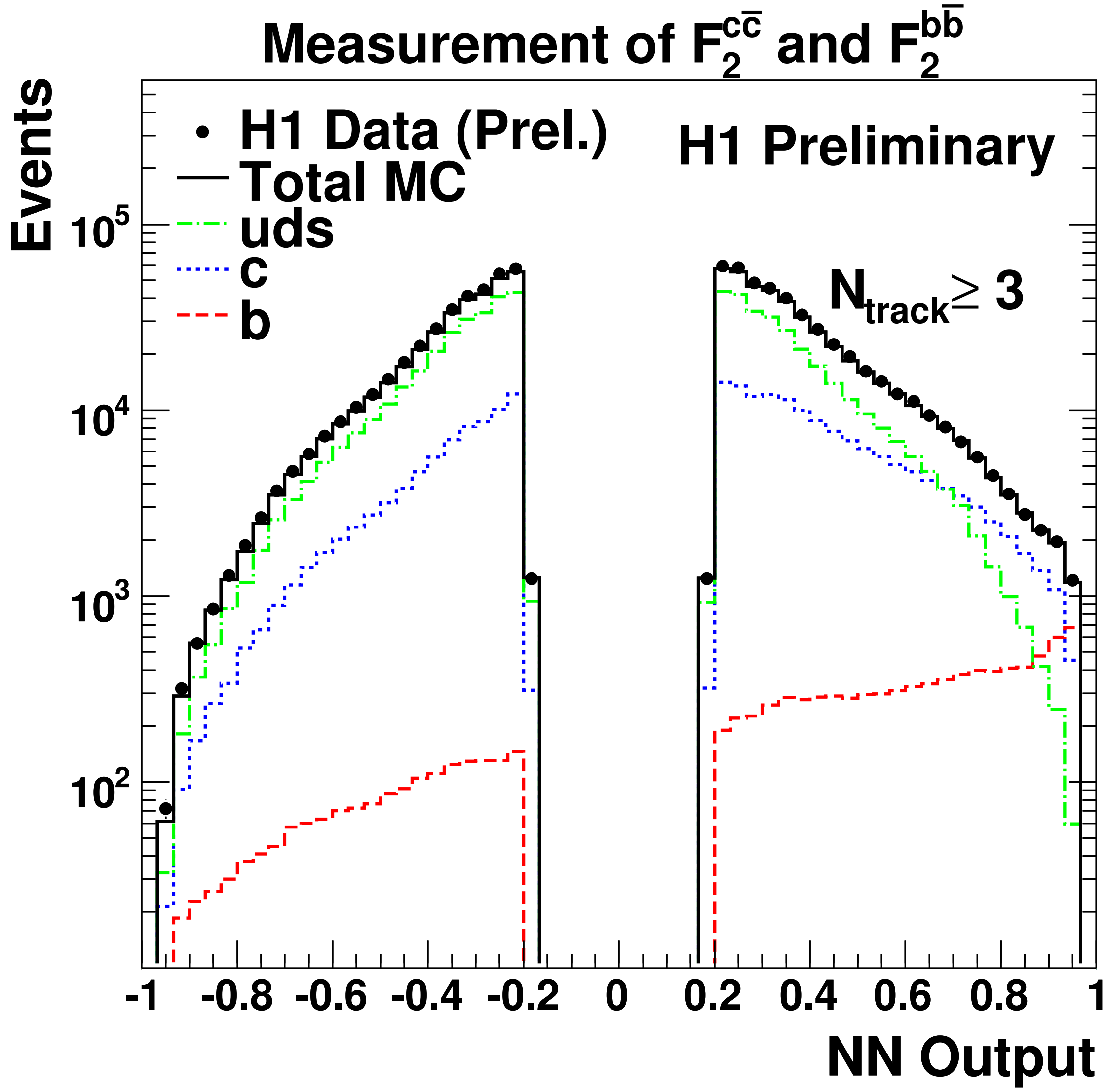

Figure 6: The output of the NN. Included in the figure is the expectation from the Monte Carlo simulation for light, c and b quarks. The contributions from the various quark flavours are shown after applying the scale factors obtained from the fit to the data.

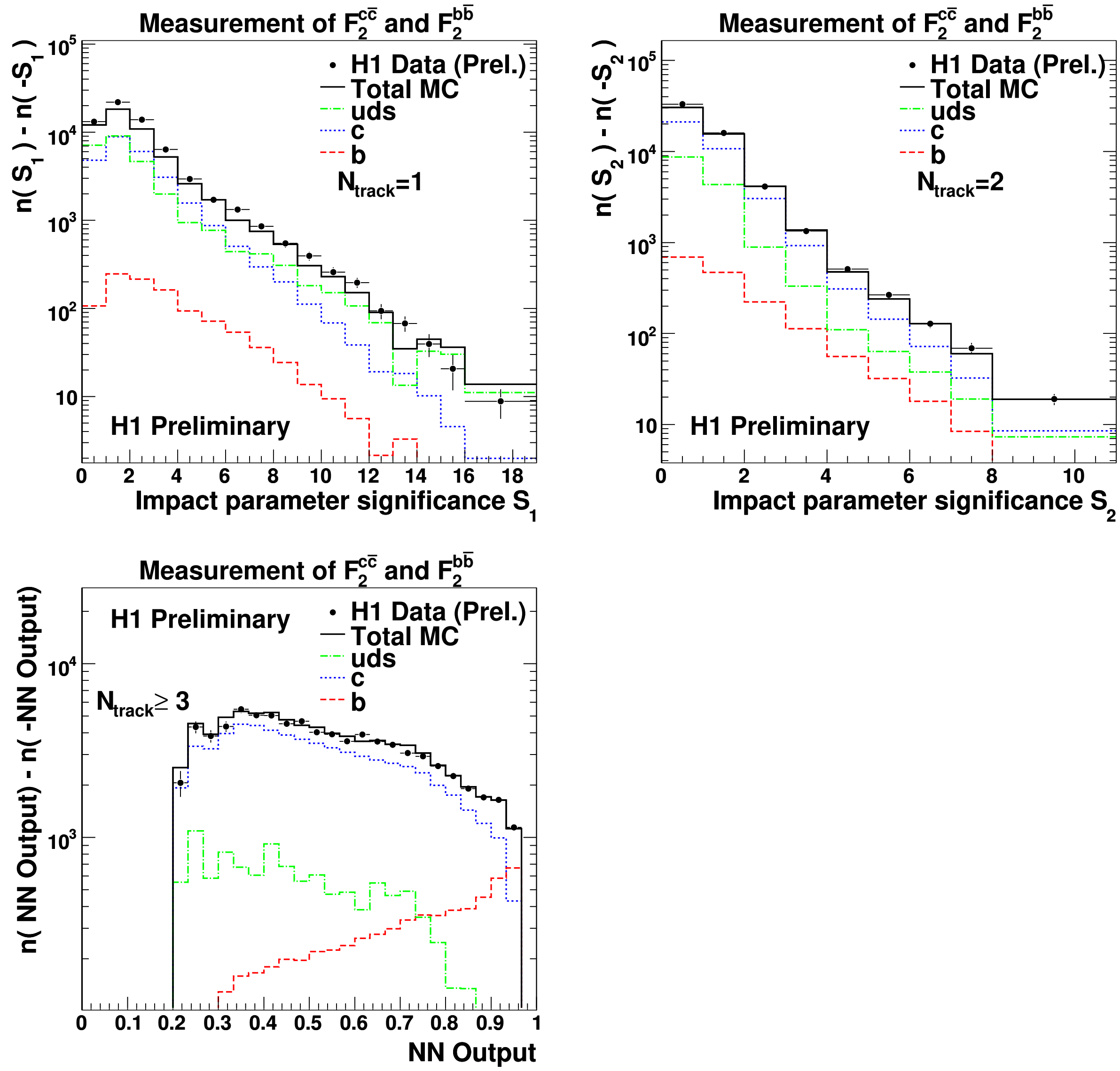

Figure 7: The subtracted significance distributions of (a) S_1 for 1 track events and (b) S_2 for 2 track events and (c) NN for $\geq$ 3 track events. Included in the figure is the result from the fit to the data of the Monte Carlo distributions of the various quark flavours.

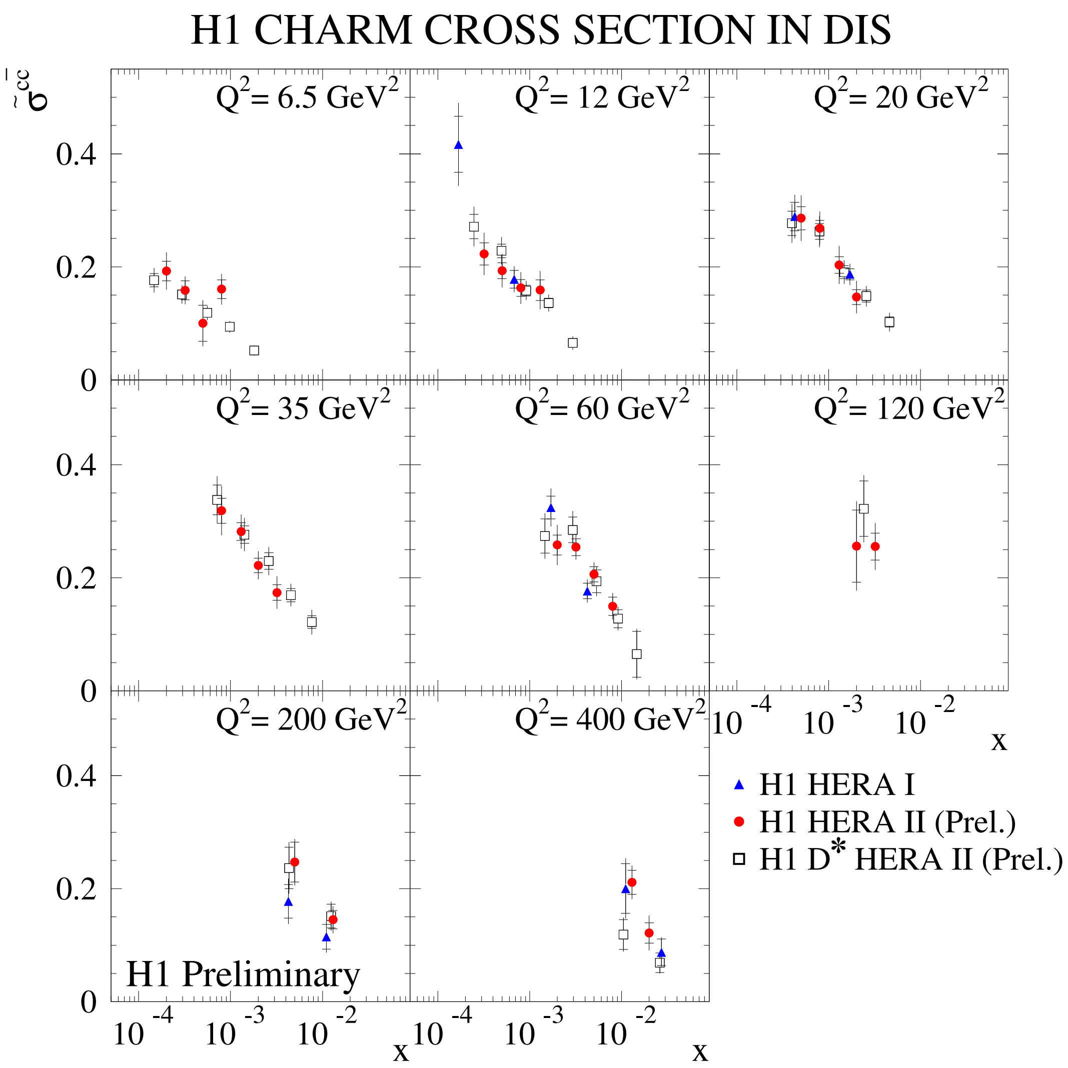

Figure 8: The measured reduced cross section $\tilde{\sigma}^{c\bar{c}}$ shown as a function of x for eight different Q^2 values. The inner error bars show the statistical error, the outer error bars represent the statistical and systematic errors added in quadrature. The measurements are compared with those from HERA I. The measurements obtained from D^* mesons from H1 [21] are also shown.

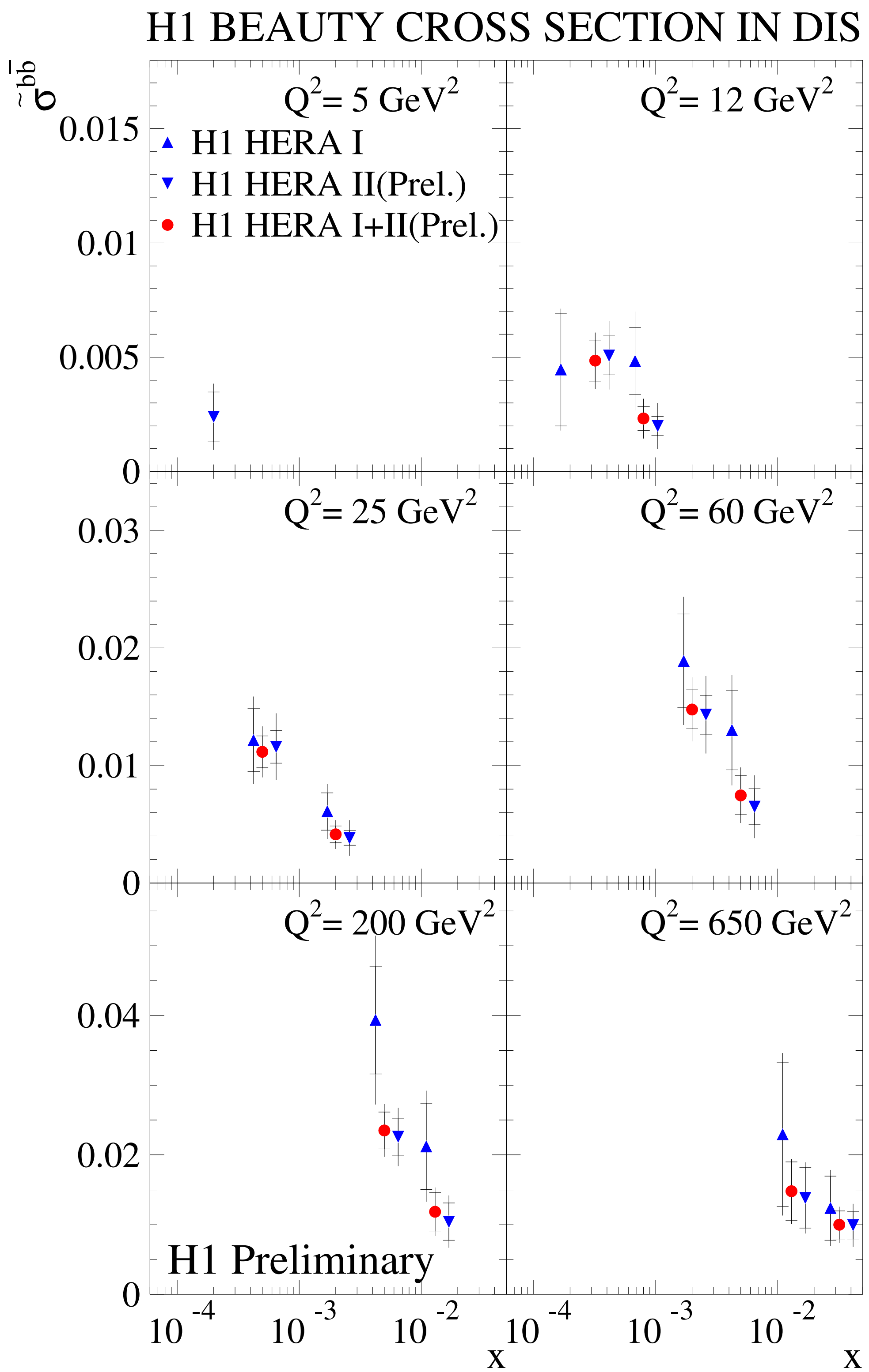

Figure 9: The measured reduced cross section $\tilde{\sigma}^{b\bar{b}}$ shown as a function of x for six different Q^2 values. The inner error bars show the statistical error, the outer error bars represent the statistical and systematic errors added in quadrature. The measurements are compared with those from HERA I, and the HERA I and HERA II averaged data are also shown.

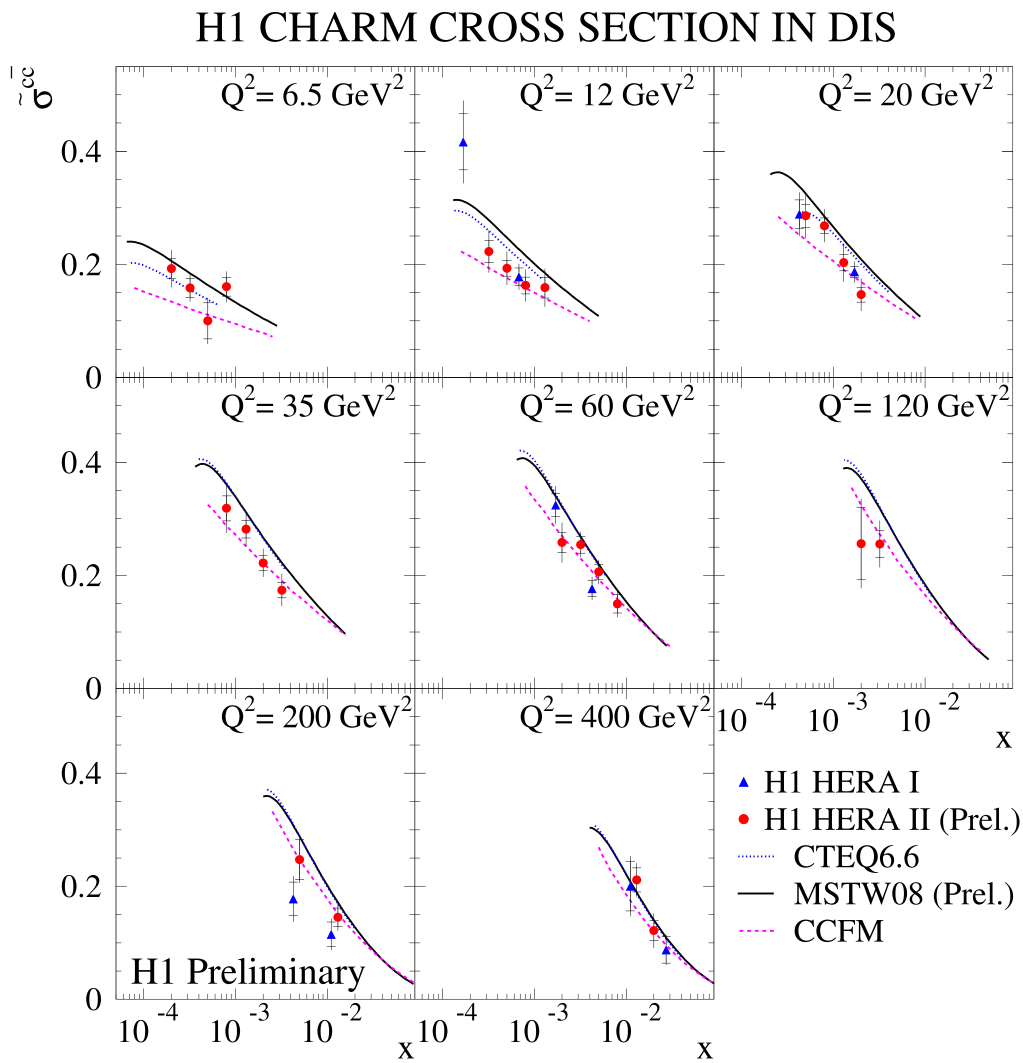

Figure 10: The measures HERA II reduced cross section $\tilde{\sigma}^{c\bar{c}}$ shown as a function of x for eight different Q^2 values. The inner error bars show the statistical error, the outer error bars represent the statistical and systematic errors added in quadrature. The predictions of QCD are also shown.

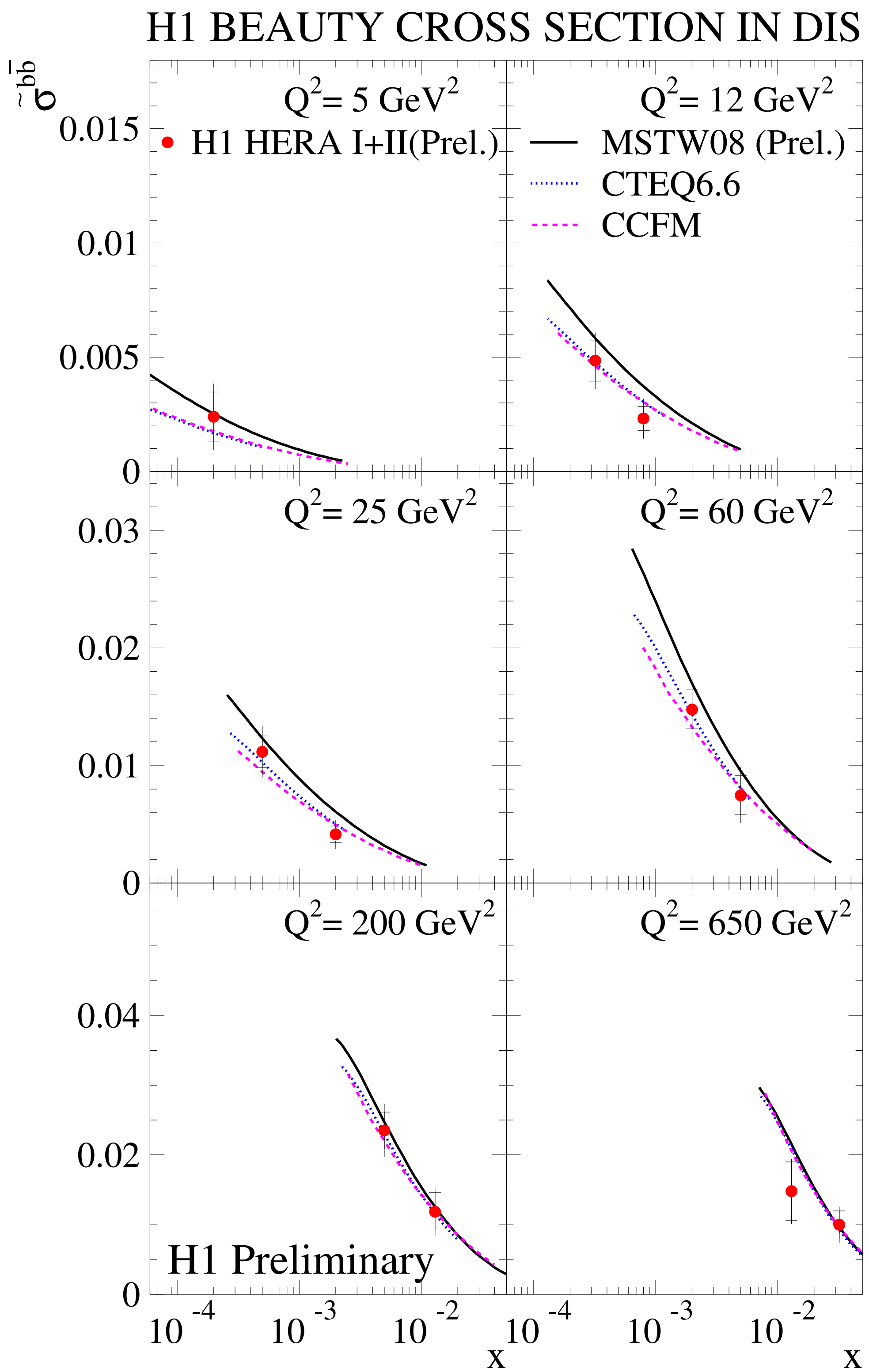

Figure 11: The measured HERA I and II averaged reduced cross section $\tilde{\sigma}^{b\bar{b}}$ shown as a function of x for six different Q^2 values. The inner error bars show the statistical error, the outer error bars represent the statistical and systematic errors added in quadrature. The predictions of QCD are also shown.

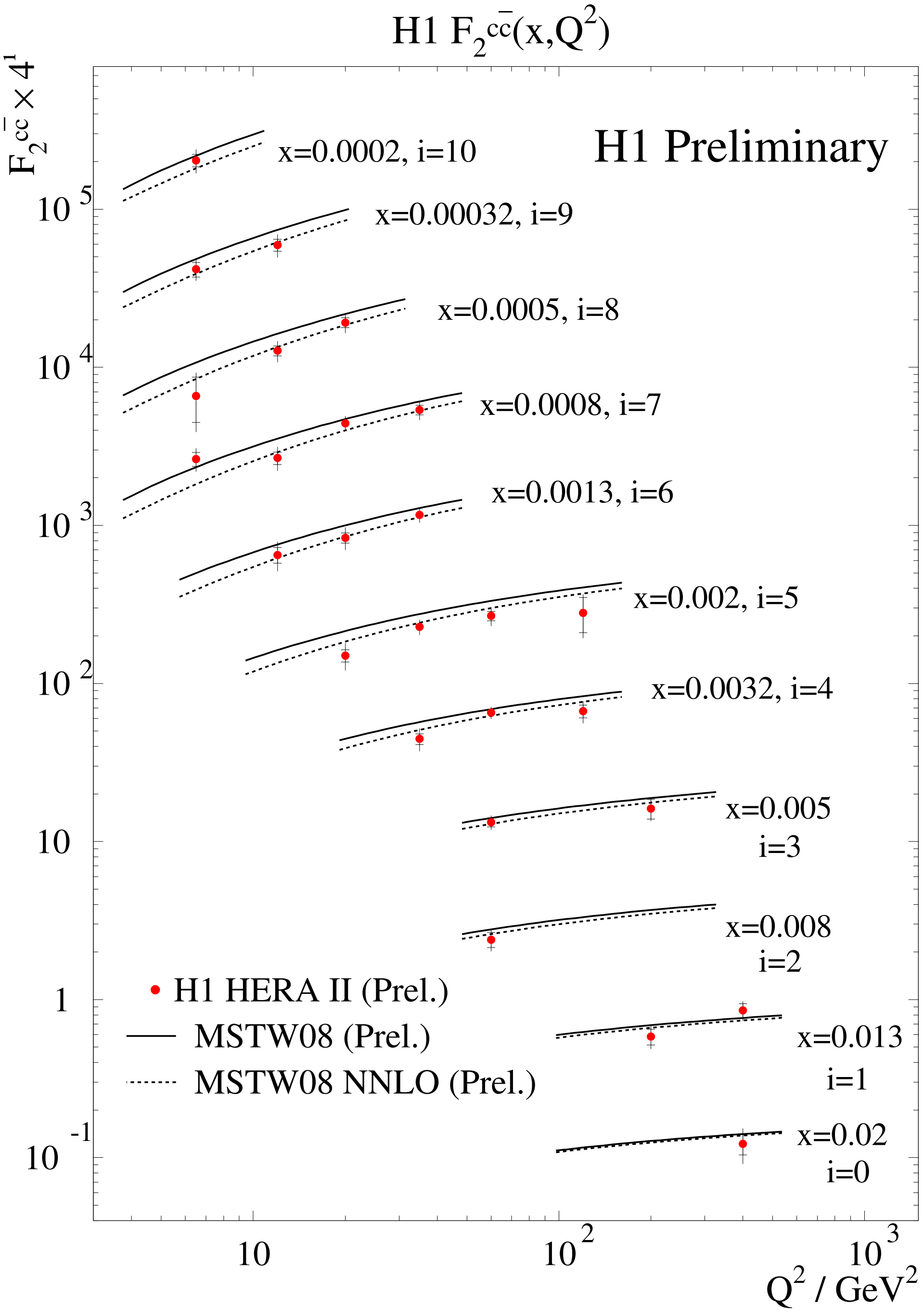

Figure 12: The measured HERA II $F_2^{c\bar{c}}$ shown as a function of Q^2 for various x values. The inner error bars show the statistical error, the outer error bars represent the statistical and systematic errors added in quadrature. The predictions of QCD are also shown.

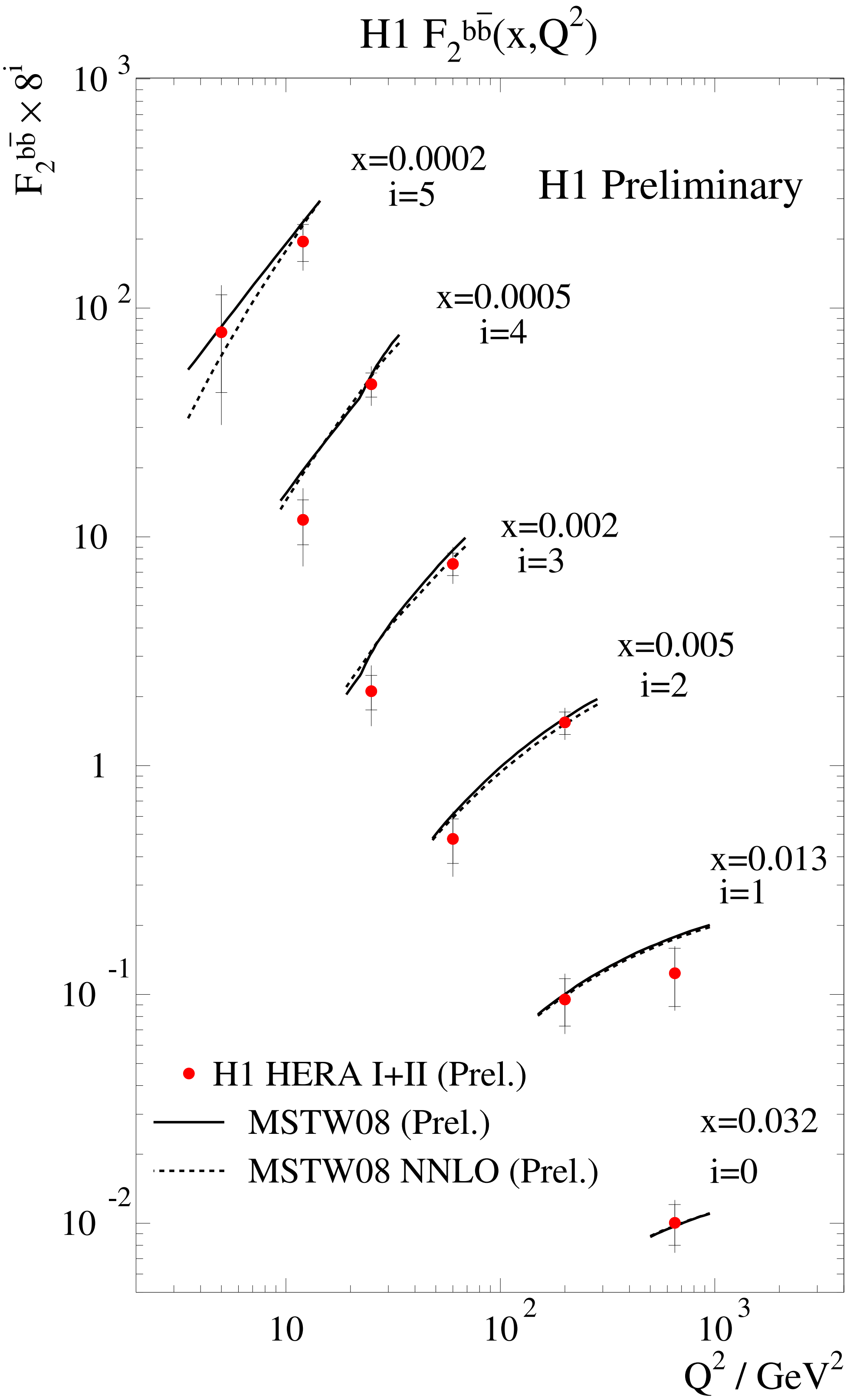

Figure 13: The measured HERA I and II averaged $F_2^{b\bar{b}}$ shown as a function of Q^2 for various x values. The inner error bars show the statistical error, the outer error bars represent the statistical and systematic errors added in quadrature. The predictions of QCD are also shown.